RSC Advances

PAPER

View Article Online
View Journal | View Issue

Cite this: *RSC Adv.*, 2021, **11**, 18945

Mn-based catalysts supported on γ-Al_2O_3, TiO_2 and MCM-41: a comparison for low-temperature NO oxidation with low ratio of O_3/NO†

Lijun Liu,[a] Boxiong Shen,*[ab] Meng Si,[a] Peng Yuan,[a] Fengju Lu,[a] Hongpei Gao,[c] Yan Yao,[d] Cai Liang[e] and Hongjie Xu[f]

Mn-Based catalysts supported on γ-Al_2O_3, TiO_2 and MCM-41 synthesized by an impregnation method were compared to evaluate their NO catalytic oxidation performance with low ratio O_3/NO at low temperature (80–200 °C). Activity tests showed that the participation of O_3 remarkably promoted the NO oxidation. The catalytic oxidation performance of the three catalysts decreased in the following order: Mn/γ-Al_2O_3 > Mn/TiO_2 > Mn/MCM-41, indicating that Mn/γ-Al_2O_3 exhibited the best catalytic activity. In addition, there was a clear synergistic effect between Mn/γ-Al_2O_3 and O_3, followed by Mn/TiO_2 and O_3. The characterization results of XRD, EDS mapping, BET, H_2-TPR, XPS and TG showed that Mn/γ-Al_2O_3 had good manganese dispersion, excellent redox properties, appropriate amounts of coexisting Mn^{3+} and Mn^{4+} and abundant chemically adsorbed oxygen, which ensured its good performance. *In situ* DRIFTS demonstrated the NO adsorption performance on the catalyst surface. As revealed by *in situ* DRIFTS experiments, the chemically adsorbed oxygen, mainly from the decomposition of O_3, greatly promoted the NO adsorption and the formation of nitrates. The Mn-based catalysts showed stronger adsorption strength than the corresponding pure supports. Due to the abundant adsorption sites provided by pure γ-Al_2O_3, under the interaction of Mn and γ-Al_2O_3, the Mn/γ-Al_2O_3 catalyst exhibited the strongest NO adsorption performance among the three catalysts and produced lots of monodentate nitrates (–O–NO_2) and bidentate nitrates (–O_2NO), which were the vital intermediate species for NO_2 formation. Moreover, the NO–TPD studies also demonstrated that Mn/γ-Al_2O_3 showed the best NO desorption performance among the three catalysts. The good NO adsorption and desorption characteristics of Mn/γ-Al_2O_3 improved its high catalytic activity. In addition, the activity test results also suggested that Mn/γ-Al_2O_3 exhibited good SO_2 tolerance.

Received 8th March 2021
Accepted 3rd May 2021

DOI: 10.1039/d1ra01820e

rsc.li/rsc-advances

1 Introduction

NO and SO_2 exhaust from coal-fired power plants can cause a number of environmental issues including acid rain and photochemical smog, as well as being severely detrimental to human health.[2–6] At present, selective catalytic reduction (SCR) of NO with NH_3 (NH_3-SCR) and subsequent wet flue-gas desulfurization technology (WFGD) have been widely used to control NO and SO_2 emissions from power plants. However, there are still several issues with this technology, such as a large carbon footprint, a relatively complex system, and poor low temperature activity.[7,8] Accordingly, developing a low-temperature efficient and simple desulfurization and denitrification system has become a research focus. Low temperature NO oxidation is regarded as a promising method for the oxidation of NO to NO_2, which can be removed simultaneously with SO_2 by subsequent wet scrubbing,[9,10] simplifying the complexity of the denitration system and achieving the goal of simultaneous desulfurization and denitrification. Thus, the oxidation of NO to NO_2 in this method is the focus of research.

Compared with noble metal catalysts such as Pt, Pd and Rh, transition metals are widely used in the research of NO oxidation due to their low prices, excellent redox performance and flexible valence states.[11,12] Among them, Mn-based catalysts exhibit good performance for NO oxidation due to its multiple oxidation states,[3,12,13] and manganese oxides are environmentally friendly active components.[4,14] Therefore, many attentions are focused on Mn-based catalysts for NO catalytic oxidation.[15–20] As a strong oxidant, ozone (O_3) could decompose to

[a]*School of Energy and Environmental Engineering, Hebei University of Technology, Tianjin, China. E-mail: shenbx@hebut.edu.cn*

[b]*School of Chemical Engineering, Hebei University of Technology, Tianjin, China*

[c]*China Huaneng Group, Clean Energy Technology Research Institute Co. Ltd, Beijing, China*

[d]*Suzhou TPRI Energy & Environment Technology Co. Ltd, Suzhou, China*

[e]*Chengdu Dongfang KWH Environmental Protection Catalysts Co. Ltd, Chengdu, China*

[f]*Xi'an Thermal Engineering Institute, Xi'an, China*

† Electronic supplementary information (ESI) available. See DOI: 10.1039/d1ra01820e

oxygen without producing self-derived byproducts,[21,22] and is widely used to oxidize pollutants. However, direct ozonation is not recommended, as it consumes large amounts of ozone, and high energy consumption by ozone generating system.[23,24] This problem may be overcome through the use of catalytic ozonation, which reduces the ozone requirements compared to direct oxidation[25,26] and improve the decomposition of ozone. In the process of catalytic ozonation, the catalysts provide active sites on the surfaces to decompose ozone into free radicals, thereby enhancing the oxidation rate.[27] Previous studies showed that manganese-based catalysts had higher ozone decomposition efficiency than other transition metal-based catalysts in gaseous media.[28,29] Therefore, catalytic ozonation with Mn-based catalysts has great value to be investigated in NO control.

In particular, the researches of catalytic ozonation mainly focus on removal VOC, such as toluene,[30] benzene,[16,31] formaldehyde,[32] at reaction temperature below 100 °C. Just few studies have reported catalytic ozonation NO. Indrek *et al.*[33] found that the presence of TiO_2 could promote the catalytic destruction of ozone creating surface-bound oxygen atoms at higher temperature, thus enhancing the deep oxidation of NO. The consistent conclusion[27] was also drawn on spherical alumina, and the deep oxidation of NO was further improved with the addition of MnO_x to spherical alumina. The main reason is that the catalyst promotes the decomposition of ozone into active oxygen and then facilitates the reaction. In addition, Lin *et al.*[34] studied a series of monometallic catalysts for NO deep oxidation by ozone and found that manganese oxides displayed the highest NO deep-oxidation efficiency of 80% at $O_3/NO = 2.0$. Besides, Ce–Mn/SA (SA: spherical alumina) and Fe–Mn/SA showed good performance and excellent stability at $O_3/NO = 1.5$ for NO deep oxidation. The synthetic action of higher surface area, better pore parameters, more oxygen vacancies and the relative balance distribution between Mn^{3+} and Mn^{4+} all favored NO deep oxidation. However, these works were carried out with high ratio of O_3 ($O_3/NO > 1$) for NO removal, increasing the extremely energy consumption, thus it was imperative to reduce the amount of O_3.

Besides, active catalysts are usually supported on different supports in industrial applications, such as Al_2O_3, TiO_2, silica and zeolite, which possess high surface, strong mechanical strength and high thermal stability.[35,36] However, the supports has great impact on the catalytic performance of catalysts.[37–40] Both the nature of supports (such as surface acidity[15,41]) and the interaction between support and metal oxides would result in great influence on specific surface area, valence states and dispersion of metal oxides, surface oxygen content and redox ability of catalysts,[1,39,42,43] further affecting the catalytic performance of catalysts. As catalyst support, Al_2O_3 could provide amount adsorbed sites for surface adsorption oxygen and reactant gas,[43,44] and the interaction between manganese oxides and Al_2O_3 showed large surface area, highly dispersed MnO_x and optimum Mn^{3+}/Mn^{4+}, which all benefited to the excellent performance of Mn/Al_2O_3.[27,45,46] The interaction between manganese oxides and TiO_2, could improve the acidic strength and redox properties,[41,42] thus Mn/TiO_2 catalyst also showed good NO conversion performance. MCM-41 with high specific area and porosity,[28] is also used as catalyst support.[47,48] Therefore, it is necessary to investigate the NO oxidation behavior over Mn-based catalysts with different supports in the presence of ozone. TiO_2, γ-Al_2O_3 and MCM-41 were selected as supports for NO conversion in this research.

In this work, the performance of Mn-based catalysts prepared with γ-Al_2O_3, TiO_2 and MCM-41 as supports for ozone-assisted NO catalytic oxidation at low temperature (80–200 °C) were investigated. Unlike previous studies, the low ratio of O_3/NO was used to participate in NO catalytic oxidation ($O_3/NO < 1$). Meanwhile, various characterization methods were performed to investigate the physicochemical properties of catalysts, and the *in situ* diffuse reflectance infrared Fourier transform spectroscopy (*in situ* DRIFTS) was used to study the change of intermediate species on the catalyst surface under different atmosphere, and further found the difference of NO adsorption on the Mn-based catalysts. This study obtains high NO oxidation efficiency at low O_3 concentration, and provides theoretical support for the selection of catalyst support.

2. Material and methods

2.1. Chemicals

Manganese acetate ($Mn(CH_3COOH)_2 \cdot 4H_2O$), MCM-41 and titanium dioxide (TiO_2) were obtained from Fengchuan Chemical Reagent Technologies Co., Ltd in Tianjin, China. Alumina was purchased from Jingjing New Material Co., Ltd in Jiangsu, China. All chemicals used were of AR grade and no further purified. Some parameters of pure supports were shown in Table 1. In addition, the XRD profiles and N_2 adsorption–desorption isotherms and pore size distribution curves of γ-Al_2O_3, TiO_2 and MCM-41 were shown in Fig. 3 and 4, which were similar to the corresponding Mn-based catalysts.

2.2. Catalyst preparation

All catalysts were prepared *via* the impregnation method. The catalysts prepared from TiO_2, alumina and MCM-41 supports

Table 1 Parameters of pure supports

Sample	Crystal phase	Particle size (nm)	Material form	BET surface area ($m^2\ g^{-1}$)	Pore volume ($cm^3\ g^{-1}$)	Average pore diameter (nm)
γ-Al_2O_3	Al_2O_3	20	Powder	204.7	0.53	10.4
TiO_2	Anatase	10–25	Powder	122.5	0.49	16.1
MCM-41	SiO_2	100–1000	Powder	672.9	0.68	4.0

were denoted as Mn/γ-Al_2O_3, Mn/TiO_2 and Mn/MCM-41, respectively. The preparation procedure for a given catalyst sample was as follows: first, $Mn(CH_3COOH)_2 \cdot 4H_2O$ was dissolved ultrasonically in 80 mL deionized water at room temperature. The corresponding mass support was then added to the solution such that the mass fraction of Mn to the support was 5 wt% and stirred for another 6 h. After refluxing in a water-bath at 80 °C for 4 h, the solid was dried at 110 °C overnight and calcined in air at 500 °C for 4 h at a temperature ramp rate of 5 °C min^{-1}. Finally, the samples obtained using this method were crushed and sieved to 40–60 mesh.

2.3. Catalyst characterization

The reduction properties of the catalysts in H_2 were obtained *via* H_2-TPR measurements on a PCA-1200 chemisorption analyzer (Builder, China). In each run, 150 mg of catalyst was used, which was pretreated to 300 °C in a flow of pure N_2 (50 mL min^{-1}) for 90 minutes and cooled to room temperature before being exposed to a flow of 10% H_2/N_2 (30 mL min^{-1}) and heated to 900 °C at a rate of 10 °C min^{-1}. NO-TPD was performed using the same instrument as the H_2-TPR. Typically, 150 mg catalysts was pretreated in 50 mL min^{-1} N_2 for 90 minutes at 300 °C and then treated in a flow of 5% NO/N_2 (50 mL min^{-1}) for 60 minutes at room temperature. The residual NO was purged by pure N_2 and the catalyst was heated to 900 °C in N_2 (30 mL min^{-1}) at a rate of 10 °C min^{-1}.

The specific surface areas of the catalysts were measured by the standard BET method with N_2 adsorption using an ASAP 2020 HD88 (Micromeritics, USA). XPS analysis was performed on an ESCALAB 250Xi (ThermoFischer, USA) scanning X-ray microprobe using Al Kα radiation (1486.6 eV) as the excitation source. Binding energies were calibrated relative to the C 1s peak from carbon contamination at 284.8 eV. The crystal structures of the catalysts were recorded using a D8 Discover (Bruker, Germany) XRD with Cu Kα radiation in the 2θ range from 10° to 90°. Thermogravimetric analysis (TG-DTG) experiments were performed on a SDT-Q600 (TA Instruments, USA) instrument under pure nitrogen flow (100 mL min^{-1}) to study the weight changes with temperature. The samples were heated from room temperature to 850 °C at 10 °C min^{-1}. Scanning electron microscopy coupled with energy dispersive spectrometer (SEM-EDS) (Hitachi, Japan) was applied to verify the dispersion of Mn on the catalysts.

Finally, the *in situ* DRIFTS were investigated using a Tendor II (Bruker, Germany) FTIR spectrometer equipped with an MCT/A detector cooled by liquid nitrogen and an *in situ* DRIFT accessory. Prior to experiments, the catalyst was pretreated at 300 °C in N_2 for 1 h and then cooled to the desired temperature. Background spectra were collected with the pretreated catalyst sample in a reaction cell containing ZnSe windows under N_2 flow at the reaction temperature. Subsequently, the reactant gas mixtures were introduced into the cell and DRIFTS spectra were recorded from 600 to 4000 cm^{-1} with a resolution of 4 cm^{-1}.

2.4. Catalytic performance tests

The O_3-assisted catalytic oxidation of NO was plain homogenous gas phase reaction and carried out in a fixed bed quartz reactor (i.d. = 8 mm). Catalyst, supported by silica wool, was added into the reactor at a gas hourly space velocity (GHSV) of 24 000 h^{-1} and the reactor temperature was set by means of a temperature controller. Ozone was generated from pure O_2 using an ozone generator and its concentrations were measured using a GM-6000-OEM ozone detector (ANSEROS, Germany). The experimental system was connected with corrosion-resistant materials, and no gas leakage was detected during the whole experiment. Quantitative analysis of the reaction products was carried out using a KM940 flue gas analyzer (Kane, England). The reaction gas consisted of a 500 ppm NO, O_3 (the molar ratio of $O_3/NO < 1$), 5 vol% O_2, and N_2 (as balance). The total flowrate was 400 mL min^{-1}. The NO conversion rate was calculated using the following formula:

$$\text{NO conversion } (\%) = \left(1 - \frac{[NO]_{out}}{[NO]_{in}}\right) \times 100\% \quad (1)$$

where $[NO]_{in}$ and $[NO]_{out}$ are the inlet and outlet concentrations of NO, respectively.

3. Results and discussion

3.1. Catalytic performance

The results of NO conversion over single catalysts (Mn/γ-Al_2O_3, Mn/TiO_2, Mn/MCM-41), single O_3 ($0.5O_3$: the molar ratio of $O_3/NO = 0.5$), and the combination of catalysts and O_3 (Mn/γ-Al_2O_3 + O_3, Mn/TiO_2 + O_3, Mn/MCM-41 + O_3) between 80–200 °C were shown in Fig. 1(a). It could be seen that in the absence of O_3, the NO conversion increased with temperature, and Mn/γ-Al_2O_3 exhibited better catalytic performance than that of other two catalysts. But overall, these catalysts presented a relative low NO conversion at test temperature. The NO conversion by single O_3 was much higher than that of single catalyst and maintained at about 45%. However, NO conversion decreased slightly as temperature increase, which was because the decomposition of O_3 enhanced with the increase of temperature. Notably, with the participation of O_3, the O_3-assisted NO conversion of three catalysts significantly enhanced, demonstrating that O_3 could apparently improve NO catalytic oxidation. For instance, the NO conversion over Mn/γ-Al_2O_3 increased from 7% to 62% after adding O_3 at 140 °C. Moreover, the catalyst-O_3 combination exhibited better activity than O_3 alone. Besides, it could be observed that with or without O_3, Mn/γ-Al_2O_3 presented the best performance among the three catalysts, followed by Mn/TiO_2. The similar results could be found when the molar ratio of $O_3/NO = 0.3$ (Fig. 1(a)) or 0.7 (Fig. 1(e)).

In order to study the synergistic effect between catalyst and O_3, the results of catalyst oxidation, sole ozonation and catalyst-O_3 composite oxidation were compared, as shown in Fig. 1(b)–(d). Meanwhile, the synergistic factor was calculated according to the following formula:

$$\varepsilon\ (\%) = \eta_{catalyst/O3} - (\eta_{catalyst} + \eta_{O3})$$

where ε (%) was the synergistic factor, $\eta_{catalyst/O3}$ was the NO conversion of catalyst–O_3 system, $\eta_{catalyst}$ and η_{O3} represented the NO conversion of catalyst system and O_3 system

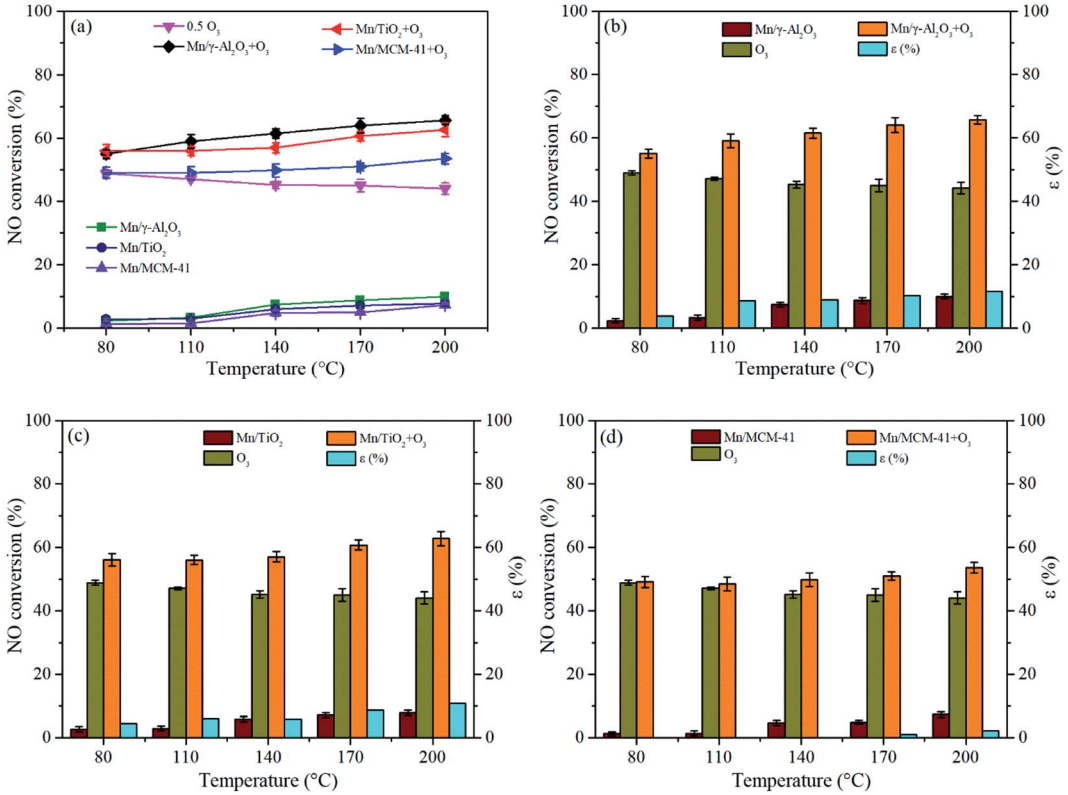

Fig. 1 NO conversion over $0.5O_3$ (the molar ratio of O_3/NO = 0.5), Mn/γ-Al_2O_3, Mn/TiO_2, and Mn/MCM-41 catalysts and the catalyst–O_3 combination (a); synergistic effect of Mn/γ-Al_2O_3 and O_3 (b); synergistic effect of Mn/TiO_2 and O_3 (c); synergistic effect of Mn/MCM-41 and O_3 (d). Other reaction conditions were as follows: NO = 500 ppm, O_2 = 5 vol%, GHSV = 24 000 h^{-1}, T = 140 °C.

respectively. According to Fig. 1(b) and (c), it could be found that there was synergistic effect between Mn/γ-Al_2O_3 and O_3, and Mn/TiO_2 and O_3, respectively. With the increasing temperature, the synergistic factor also increased from 4% to 12% and 5% to 11% for Mn/γ-Al_2O_3 and Mn/TiO_2, respectively, but overall, the synergistic factor of Mn/γ-Al_2O_3 was slightly higher than Mn/TiO_2. However, there was no significant synergistic effect between Mn/MCM-41 and O_3 as shown in Fig. 1(d), whence the maximum synergistic factor was only 2% at 200 °C. In addition, Fig. 1(b)–(d) and (f)–(h) also demonstrated that when the molar ratio of O_3/NO was 0.3 or 0.7, the synergistic effect between Mn/γ-Al_2O_3 and O_3 was more obvious than Mn/TiO_2 and O_3, and Mn/MCM-41 and O_3. Based on the above results, it could be inferred that the supports would affect the catalytic activity of Mn-based catalysts. Thus, it was essential to analyze the physicochemical properties of catalysts with different supports.

3.2. Results of catalyst characterization

3.2.1. BET and XRD analysis. The N_2 adsorption–desorption isothermal and pore size distribution plots of Mn/γ-Al_2O_3, Mn/TiO_2 and Mn/MCM-41 were depicted in Fig. 2. As shown in

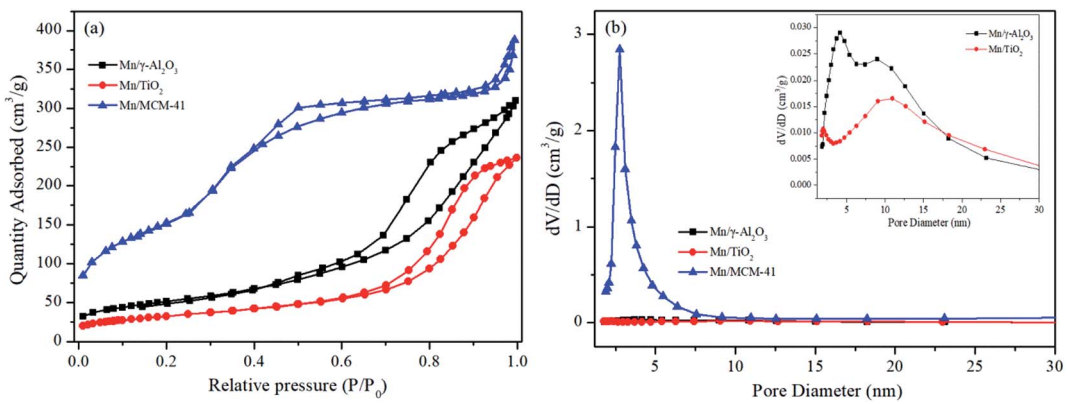

Fig. 2 N_2 adsorption–desorption isotherms (a) and pore size distribution curves (b) of the Mn/γ-Al_2O_3, Mn/TiO_2 and Mn/MCM-41 catalysts.

Table 2 BET surface area and pore parameters, H_2 consumption amounts and the Mn loading of different Mn-based catalysts

Catalysts	BET surface area ($m^2\ g^{-1}$)	Pore volume ($cm^3\ g^{-1}$)	Average pore diameter (nm)	H_2 consumption ($\mu mol\ g^{-1}$)	Mn loading[a] (wt%)
Mn/γ-Al_2O_3	183.9	0.45	9.7	303	5.28
Mn/TiO_2	115.9	0.36	12.6	726	5.11
Mn/MCM-41	554.4	0.52	3.8	76	5.15

[a] Determined by ICP-OES.

Fig. 2(a), all samples presented a typical characteristic mesoporous materials with the type-IV adsorption–desorption isotherms, identified by the International Union of Pure and Applied Chemistry (IUPAC). Exceptionally, Mn/γ-Al_2O_3 and Mn/TiO_2 exhibited H_3 hysteresis loops in the region of high relative pressures (0.6–1.0), implying the irregular pore structure with flake grains or narrow slit-like shapes.[12] In Fig. 2(b), Mn/MCM-41 showed one single narrow peak in the range of 2–5 nm, suggesting that Mn/MCM-41 possessed relative uniform mesopore size distributions. In Fig. 2(b) (inset), the maximum pore size of Mn/TiO_2 centered at 8–15 nm, while that of Mn/γ-Al_2O_3 mainly centered at 5–15 nm. The BET surface areas and pore parameters for Mn/γ-Al_2O_3, Mn/TiO_2 and Mn/MCM-41 were listed in Table 2. It could be found that Mn/MCM-41 displayed the highest BET surface area among the three catalysts, around three times as high as that of Mn/γ-Al_2O_3 and five times that of Mn/TiO_2. The main reason for the difference of BET specific surface areas was probably attributed to the different supports, which was of vital importance for catalyst physical properties.[49] Combined with catalytic oxidation results that Mn/γ-Al_2O_3 exhibited the highest NO oxidation efficiency, it could be indicated that the surface area was not the major factor in NO oxidation.

The XRD patterns of the three catalyst samples were shown in Fig. 3. For Mn/TiO_2, only the pure anatase phase was observed, with diffraction angles located at 25.3°, 37.8°, 48.0°, 53.9°, 55.1°, 62.7°, 68.8°, 70.3°, 75.0°, and 82.7° (JCPDS 21-1272). For MCM-41, the only diffraction peak, at $2\theta = 22.0°$, was correlated to SiO_2 (JCPDS 29-0085). For Mn/γ-Al_2O_3, the weak diffraction peaks for Al_2O_3 appeared at 37.6°, 45.9°, and 67.0° (JCPDS 10-0425). No crystalline manganese oxide peaks were found in the XRD spectra of any of the catalysts, probably due to the low loading or high dispersion in amorphous or microcrystalline on the surface of catalyst. The Mn elemental mapping images of Mn/γ-Al_2O_3, Mn/TiO_2 and Mn/MCM-41 was depicted in Fig. 2. It showed that Mn in Mn/γ-Al_2O_3, Mn/TiO_2 and Mn/MCM-41 were all highly dispersed. In addition, The Mn contents of the three catalysts were detected by ICP-OES that they are similar to the expected Mn/support mass ratio (~5%), and the results are shown in Table 2.

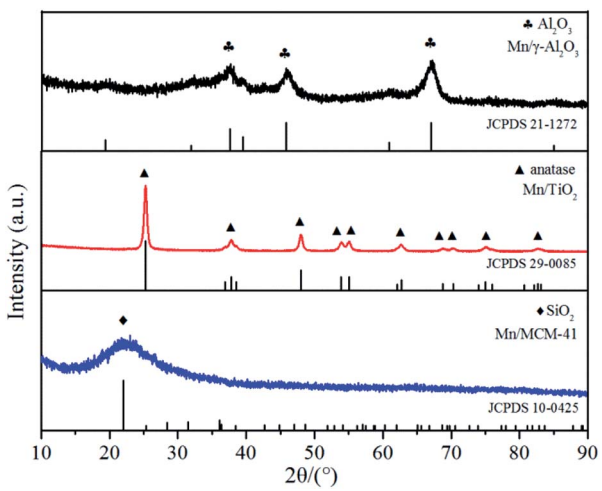

Fig. 3 XRD profiles of Mn/γ-Al_2O_3, Mn/TiO_2 and Mn/MCM-41 catalysts.

3.2.2. H_2-TPR analysis. The redox properties was the vital factor for NO oxidation, and evaluated by H_2-TPR. Fig. 4 showed the H_2-TPR profiles of three catalysts with different support, whence it could be seen from Fig. 4(a) that two distinct reduction peaks were present, at 380 °C and 556 °C for Mn/TiO_2, and at 350 °C and 620 °C for Mn/MCM-41. The reduction stages were related to the valence evolution of manganese.[50,51] According to previous studies,[4,5,52] the reduction process was generally regarded as MnO_2 or Mn_2O_3 → Mn_3O_4 and Mn_3O_4 → MnO. The second peak was dominant for Mn/TiO_2 and the first was dominant for Mn/MCM-41, which indicated that Mn on Mn/TiO_2 was mainly in low valence state and Mn on Mn/MCM-41 was mainly in high valence state. However, Mn/γ-Al_2O_3 displayed three reduction peaks, at 350 °C, 460 °C, and 715 °C, representing the reduction steps MnO_2 → Mn_2O_3 → Mn_3O_4 → MnO[50] occurring from 100 °C to 800 °C, indicating that Mn existed on the surface of Mn/γ-Al_2O_3 in various valence states. Besides, the first two peaks were dominant for Mn/γ-Al_2O_3. From Fig. 4(b), it was clear that the reduction peak of Mn/MCM-41 was weaker than Mn/γ-Al_2O_3 and Mn/TiO_2, consisting with Table 2 that Mn/MCM-41 consumed the least amount of H_2. Thus, the redox ability of Mn/MCM-41 was the worst. Although Mn/TiO_2 possessed the largest H_2 consumption, it was mainly concentrated in the high temperature range above 500 °C, which was opposite to that of Mn/γ-Al_2O_3. According to previous reports, the lower initial reduction temperature suggested better redox characteristics for catalysts.[53] In addition, it should be noted that below 480 °C (inset), Mn/γ-Al_2O_3 showed larger peak area and lower initial reduction temperature, followed by Mn/TiO_2 and then Mn/MCM-41. Therefore, the redox capability order of catalysts at low temperature was in the following

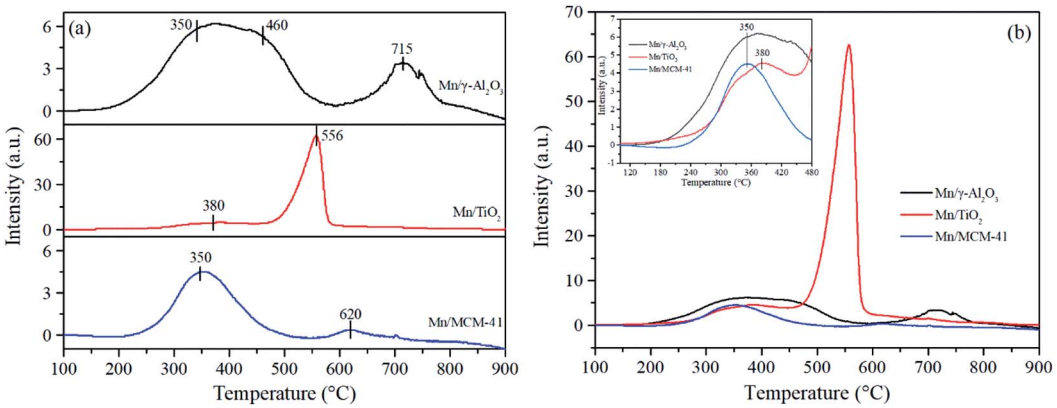

Fig. 4 H_2-TPR profiles of the Mn/γ-Al_2O_3, Mn/TiO_2 and Mn/MCM-41 catalysts (a) and (b).

sequence: Mn/γ-Al_2O_3 > Mn/TiO_2 > Mn/MCM-41, which was consistent with the results of catalytic activity.

3.2.3. XPS analysis. The interaction between metal oxides and supports will affect the oxidation state of metal oxides, and further affect the activity of catalyst. Therefore, XPS technique was employed to investigate the element chemical state of Mn-based catalysts with different supports. The surface chemical states of Mn $2p_{3/2}$ and O 1s for the following samples: Mn/γ-Al_2O_3, Mn/γ-Al_2O_3 after ozone adsorption (O_3–Mn/γ-Al_2O_3), Mn/γ-Al_2O_3 after the reaction (NO + O_3–Mn/γ-Al_2O_3), Mn/MCM-41, and Mn/TiO_2 were analyzed by XPS. Fig. 5(a) exhibited the XPS spectra of Mn $2p_{3/2}$, the binding energy at 640.8 eV, corresponding to Mn^{2+},[54] was only observed on Mn/TiO_2. The peak at 641.8–641.9 eV corresponded to Mn^{3+},[11,27] whereas the signal at 643.2 eV and 646.0 eV could be assigned to Mn^{4+}.[49,55,56] Both Mn^{3+} and Mn^{4+} were found on the surfaces of Mn/γ-Al_2O_3 and Mn/TiO_2. There was also Mn^{7+} at 647.3 eV for Mn/γ-Al_2O_3.[27] For Mn/MCM-41, Mn^{4+} (642.9 eV) and Mn^{7+} (646.9 eV) were detected on the surface. Surface valence compositions of O 1s and Mn $2p_{3/2}$ for different catalysts were listed in Table 3. It could be found from Table 3 that the ratio of Mn^{3+}/Mn in Mn/TiO_2 was the highest, followed by Mn/γ-Al_2O_3, while for Mn-MCM-41, there was no Mn^{3+} and the ratio of Mn^{4+}/Mn was the highest. This was consistent with the result of H_2-TPR. According to the result of Fig. 1 that Mn/γ-Al_2O_3 exhibited the highest activity, followed by Mn/TiO_2, it could be inferred that proper ratio of Mn^{3+} and Mn^{4+} was more beneficial to the catalytic oxidation of NO.

Previous report revealed that Mn^{3+}–O was easy to break, furthermore, the presence of Mn^{3+} was more conducive to the combination of O and NO, and then promoted the formation and release of NO_2 product.[57] Moreover, a portion of Mn^{3+} neighbored with oxygen vacancies, which could accelerate the decomposition of O_3 into adsorbed oxygen. When the oxygen vacancies were filled up with adsorbed oxygen, Mn^{3+} would be oxidized into unstable Mn^{4+} to balance charge neutralization and produced more active sites of redox couples on the surface of catalysts.[58,59] The above analysis indicated that the coexistence of Mn^{3+} and Mn^{4+} could provide more active sites and further promote NO oxidation in the presence of ozone, which was consistent with result of Fig. 1 that Mn/γ-Al_2O_3 and Mn/TiO_2 with Mn^{3+} and Mn^{4+} exhibited higher activity than Mn-MCM-41. Eqn (2) and (3) may represent ozone decomposition reactions on the surface of Mn-based catalysts:

$$[Mn^{3+}] + O_3 \rightarrow O_2 + O_{ads}^{-}\text{–}[Mn^{4+}] \quad (2)$$

$$O_{ads}^{-}\text{–}[Mn^{4+}] + O_3 \rightarrow 2O_2 + [Mn^{3+}] \quad (3)$$

$$O_{ads}^{-}\text{–}[Mn^{4+}] + NO \rightarrow NO_2 + [Mn^{3+}] \quad (4)$$

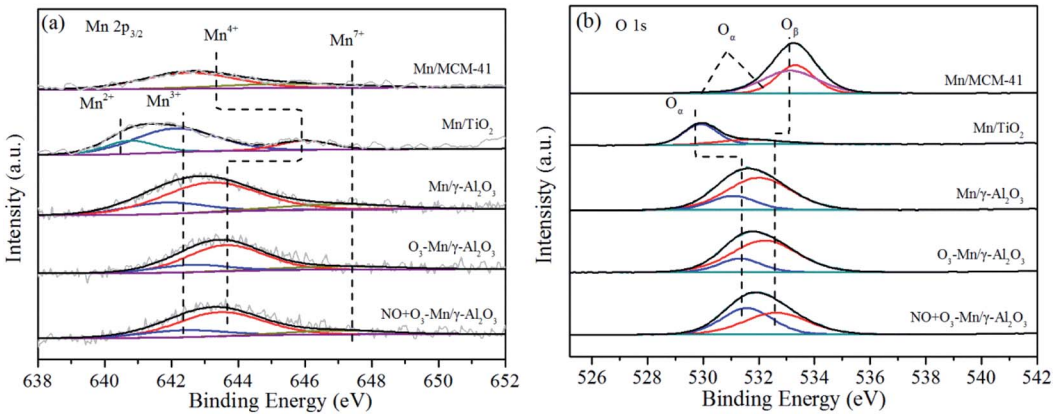

Fig. 5 XPS spectra of the Mn/TiO_2, Mn/γ-Al_2O_3, and Mn/MCM-41 catalysts: (a) Mn $2p_{3/2}$ and (b) O 1s.

Table 3 Surface valence compositions of Mn $2p_{3/2}$ and O 1s for different samples

	Mn $2p_{3/2}$				O 1s	
Samples	Mn^{2+}/Mn	Mn^{3+}/Mn	Mn^{4+}/Mn	Mn^{7+}/Mn	O_α/O	O_β/O
Mn/γ-Al_2O_3	—	0.21	0.66	0.13	0.23	0.77
Mn/TiO_2	0.18	0.66	0.16	—	0.70	0.30
Mn/MCM-41	—	—	0.77	0.23	0.47	0.53
O_3–Mn/γ-Al_2O_3	—	0.18	0.69	0.13	0.21	0.79
NO + O_3–Mn/γ-Al_2O_3	—	0.20	0.67	0.13	0.49	0.51

Comparing between the different Mn/γ-Al_2O_3 based samples, the ratios of Mn^{3+}/Mn decreased in the following sequence: Mn/γ-Al_2O_3 > NO + O_3–Mn/γ-Al_2O_3 > O_3–Mn/γ-Al_2O_3, as shown in Table 3. Meanwhile, the ratio of Mn^{4+} increased after O_3 adsorption and reaction, indicating that the Mn^{3+} was oxidized to Mn^{4+} by O_3 in the flue gas *via* a transition of the Mn valance state. Reed *et al.*[60] found that the electron transfer between the catalyst and O_3 caused the decomposition of the latter into active oxygen. In addition, only a very small amount of Mn^{3+} was converted to Mn^{4+}, suggesting that Mn^{3+} and Mn^{4+} were in a dynamic transformation equilibrium state. Therefore, it might be tentatively surmised that the ozone decomposition process did followed eqn (2) and (3), whereby ozone was catalytically decomposed to active atomic oxygen,[27] which was conducive to the NO oxidation.[20]

The O 1s spectra of the Mn-based catalysts were presented in Fig. 5(b), with the valence state ratios listed in Table 3. The O 1s spectra showed two peaks for both Mn/γ-Al_2O_3 and Mn/TiO_2. The low binding energy peaks (529.9–531.6 eV) corresponded to surface lattice oxygen (O_α), and those with high binding energy (531.7–532.6 eV) assigned to surface adsorbed oxygen (O_β).[61] However, for Mn/MCM-41, three peaks were observed, which were attributed to lattice oxygen (O_α) of metal oxides (Mn–O) and Si–O and adsorbed –OH groups (O_β) at 530.9 eV, 533.3 eV and 532.8 eV,[2,3,62,63] respectively. It was widely accepted that O_β was more beneficial for the NO oxidation than O_α due to its higher mobility.[64] From the XPS analysis results in Table 3, it could be detected that Mn/γ-Al_2O_3 with the highest catalytic activity contained the largest amount of O_β. Although the content of O_β in Mn/MCM-41 was higher than that in Mn/TiO_2, there was no Mn^{3+} in Mn/MCM-41. It was likely that the combined action of O_β and Mn^{3+} made the activity of Mn/TiO_2 higher than that of Mn/MCM-41. Compared to the plain Mn/γ-Al_2O_3 catalyst, the O_β/O ratio increased slightly for O_3–Mn/γ-

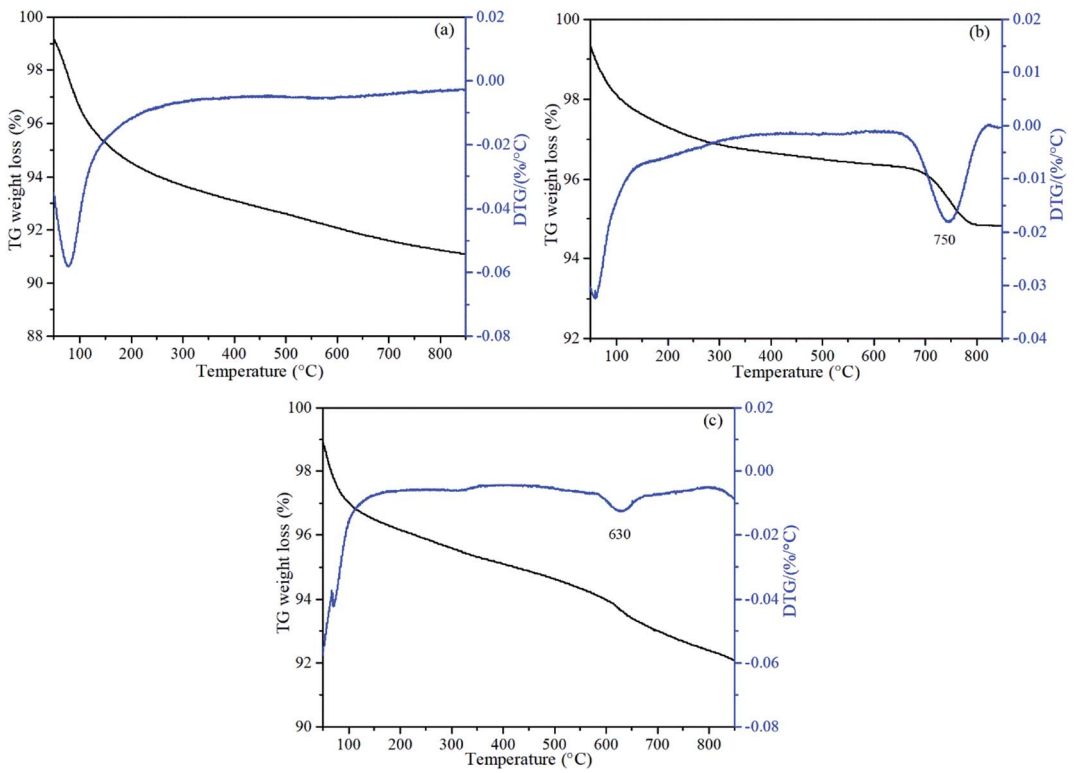

Fig. 6 TG and DTG profiles for (a) Mn/γ-Al_2O_3, (b) Mn/TiO_2 and (c) Mn/MCM-41.

Al_2O_3, which indicated that the decomposition of O_3 on the surface of catalyst generated the adsorbed oxide species *via* eqn (2). Nevertheless, the ratio O_β/O of NO + O_3–Mn/γ-Al_2O_3 significantly decreased, which might be due to the adsorbed oxygen presented on the surface of catalysts or produced by ozone decomposition were consumed *via* eqn (4). Consequently, it could be inferred that proper ratio of Mn^{3+} and Mn^{4+} and abundant O_β on the catalyst surface played the significant role in NO oxidation. Although the atomic ratio of Mn^{3+} for Mn/γ-Al_2O_3 was lower than that of Mn/TiO_2, a better NO oxidation performance was obtained with Mn/γ-Al_2O_3, which could be rationalized by the high concentration of O_β and proper ratio of Mn^{3+} and Mn^{4+} in the catalyst.

3.2.4. TGA analysis. The TG–DTG results were shown in Fig. 6, whence it could be seen that Mn-based catalysts with different supports exhibited quite different thermal stabilities. The weight loss behavior of the catalysts fell roughly into the following three stages: the initial weight loss, below 200 °C, was attributed to the desorption of physically and chemically adsorbed water; the second stage, from 200–400 °C, was attributed to the desorption of surface-active oxygen species; the third stage, above 400 °C, was due to the loss of structural oxygen in the framework of the tunnels.[65–67] In the first stage,

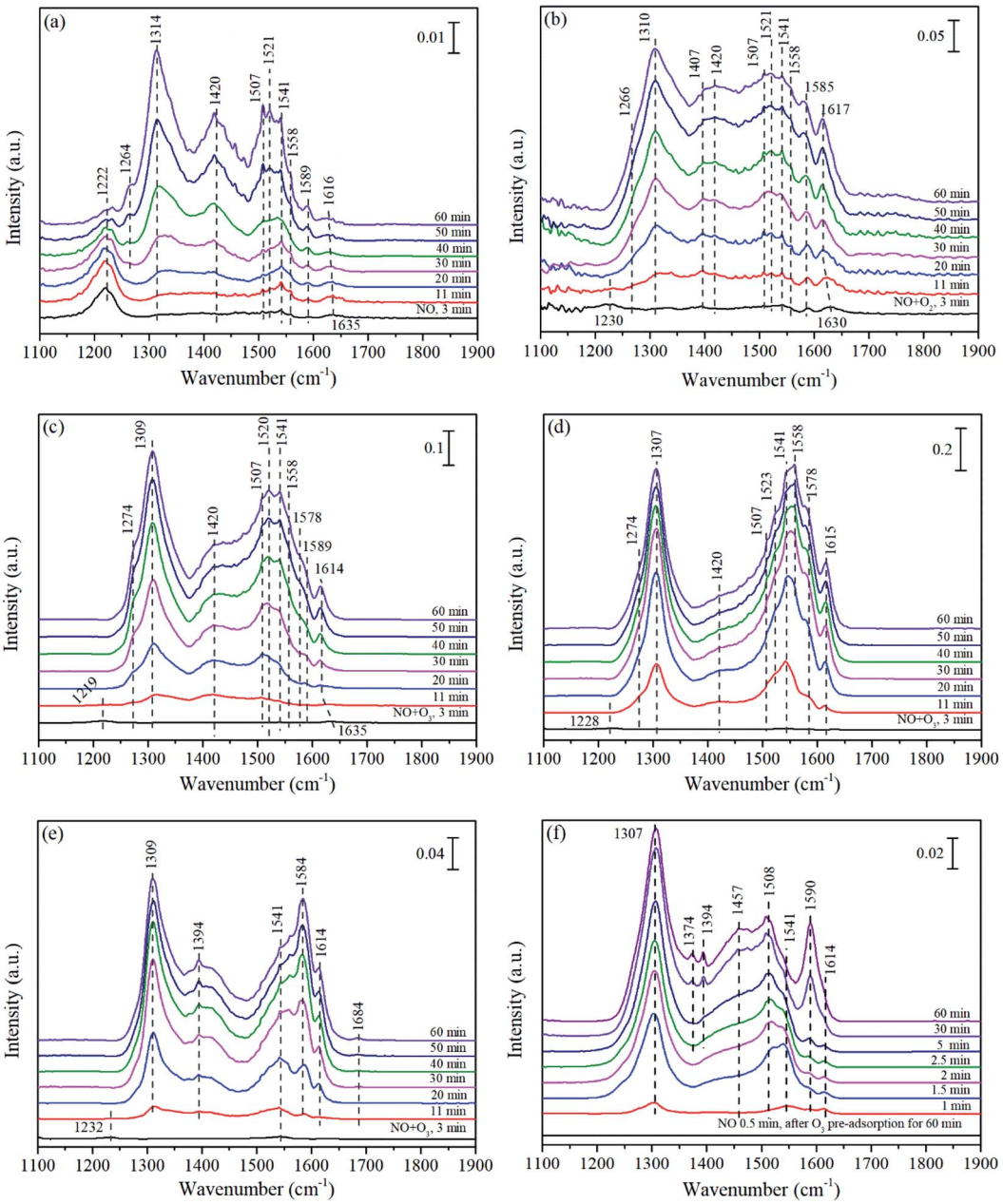

Fig. 7 *In situ* DRIFTS of Mn/γ-Al_2O_3 (a–d and f) and pure γ-Al_2O_3 (e) exposed to NO (a), NO + O_2 (b), NO + O_3 at 140 °C (c and e), NO + O_3 at 200 °C (d), and NO after O_3 pre-adsorption at 140 °C (f).

a significant weight loss was observed for all the catalysts. In the latter two stages, Mn/γ-Al_2O_3 showed a continuous weight-loss, indicating that most of the MnO_x likely existed in amorphous rather than crystalline form,[54] which was also consistent with the result of XRD and EDS mappings. For Mn/MCM-41, obvious weight loss occurred at ~630 °C, which was attributed to the transformation of MnO_2 to Mn_2O_3, whereas Mn/TiO_2 showed obvious weight loss at ~750 °C due to the transformation of Mn_2O_3 to Mn_3O_4.[54] These results suggested that Mn/TiO_2 and Mn/MCM-41 were rich in Mn^{3+} and Mn^{4+}, respectively, which was in agreement with the H_2-TPR and XPS results.

3.3. *In situ* DRIFTS

In order to study the difference of NO catalytic oxidation performance over three catalysts, the NO adsorption behavior at different atmospheres and the evolution of reaction intermediates over three catalysts were investigated *via in situ* DRIFTS experiments. For reference, the spectra of pure supports of corresponding catalysts were also studied.

3.3.1. NO adsorption over Mn/Al_2O_3 catalyst. Fig. 7 showed the NO adsorption behavior over Mn/γ-Al_2O_3 and pure γ-Al_2O_3 under different atmospheres. The *in situ* DRIFT spectra of Mn/γ-Al_2O_3 adsorbed NO at 140 °C for 60 min was shown in Fig. 7(a). In Fig. 7(a), it was seen that bridged nitrites (1222 cm^{-1})[68] was the main species at the beginning adsorption. With increasing time, the bridged nitrites decreased gradually, while the bidentate nitrates at 1541, 1558 and 1589 cm^{-1},[3,12,69,70] monodentate nitrates at 1264, 1314, 1507 and 1521 cm^{-1},[68,71–73] and monodentate nitrites at 1420 cm^{-1} (ref. 12) as well as weak bands of bridged nitrates at 1616 cm^{-1} (ref. 68) emerged and gradually increased with adsorption time. This suggested that bridged nitrites could decompose and transform to other nitrates or nitrites, facilitating the NO oxidation. Fig. 7(b) illustrated the FTIR spectra of Mn/γ-Al_2O_3 exposed to NO + O_2 at 140 °C. The weak bridged nitrites on Mn/γ-Al_2O_3 (1230 cm^{-1}) disappeared within 11 min after NO + O_2 was introduced. Furthermore, the peaks intensity associated with nitrates and nitrites in Fig. 7(b) were stronger compared with those in Fig. 7(a), indicating that O_2 could supply abundant active oxygen species and promote the NO adsorption and oxidation. Compared with Fig. 7(b), similar bands with stronger intensity could be observed in Fig. 7(c), suggesting that the oxidation of NO by O_3 was much stronger than that by O_2. Fig. 7(d) presented the FTIR spectra of Mn/γ-Al_2O_3 exposed to NO + O_3 at 200 °C. The bands in Fig. 7(d) grew faster than that in Fig. 7(c), indicating that the NO adsorption was enhanced with the increasing temperature. In the meantime, it could be detected that the relative intensity of monodentate nitrites (1420 cm^{-1}) weakened due to its conversion to the main species of mondentate nitrates and bidentate nitrates in Fig. 7(d). Combined with the result of Fig. 1(b), it could be speculated that monodentate nitrates and bidentate nitrates was the key intermediate species that promoted NO catalytic oxidation and further facilitated synergistic effect between catalyst and O_3.

Fig. 7(e) showed the FTIR spectra of pure γ-Al_2O_3 exposed to NO + O_3 at 140 °C. Obviously, after the introduction of NO + O_3, weak bridged nitrites (1232 cm^{-1}) emerged at the beginning and quickly disappeared in 11 min, followed by the appearance and rapid enhancement of monodentate nitrates (1309 cm^{-1}), bidentate nitrates (1541 and 1584 cm^{-1}) as well as monodentate nitrite (1394 cm^{-1}). In particular, weakly adsorbed NO were also observed at 1684 cm^{-1}.[6] NO was supposed to adsorb on the sites of positive charged alumina ions,[74] and then was catalytically oxidized to various nitrates and nitrites,[75] indicating that the pure γ-Al_2O_3 promoted the NO adsorption on the catalyst surface followed by the formation of nitrates. At times, it could be found that the lineshape of pure γ-Al_2O_3 were similar to that of Mn/γ-Al_2O_3 in Fig. 7(c), but the intensity was weaker than that of Mn/γ-Al_2O_3. These phenomena indicated that the addition of Mn promoted the adsorption of NO and the formation of intermediate species. Research had proved that O_3 decomposition with Mn/γ-Al_2O_3 was much higher than that with pure γ-Al_2O_3, and amount active oxygen would be produced to accelerate the oxidation of NO.[27] As revealed by XPS, the coexistence of Mn^{3+} and Mn^{4+} could promote more active sites, which accelerated the decomposition of ozone to produce active oxygen. Therefore, Mn/γ-Al_2O_3 exhibited better adsorption for NO than that of pure γ-Al_2O_3.

After O_3 pretreatment, abundant chemically adsorbed oxygen was stored on the surface of Mn/γ-Al_2O_3 as shown in Fig. 7(f). Once NO was introduced into the system, various N-species appeared and increased with time. After NO adsorption for 60 min, the peak intensity in Fig. 7(f) was stronger than that in Fig. 7(a), demonstrating that chemically adsorbed oxygen decomposed from O_3 remarkably enhanced the NO adsorption on the surface of catalysts.

3.3.2 NO adsorption over Mn/TiO_2 catalyst. Fig. 8 showed the NO adsorption behavior over Mn/TiO_2 and pure TiO_2 under different atmospheres. The *in situ* DRIFT spectra of NO over Mn/TiO_2 was shown in Fig. 8(a). As shown in Fig. 8(a), the peaks attributed to bridged nitrites and bridged nitrates were detected at 1212 cm^{-1}, 1636 and 1647 cm^{-1}, respectively. The weak bridged nitrites quickly vanished in 20 min, while bridged nitrates reached the highest intensity at 11 min and then decreased gradually with time. After that, the bidentate nitrates at 1541 and 1558 cm^{-1} and monodentate nitrates at 1487, 1507 and 1522 cm^{-1} appeared and increased gradually with time, demonstrating that bridged nitrites converted into bridged nitrates, which was then converted into bidentate and monodentate nitrates. Fig. 8(b) displayed the DRIFT spectra of Mn/TiO_2 exposed to NO + O_2. It was obviously that the peak at 1308 cm^{-1} assigned to monodentate nitrates appeared and enhanced with temperature, while the bridged nitrites at 1212 cm^{-1} were not observed, probably due the rapid conversion of bridged nitrites to monodentate nitrates. Meanwhile, the intensity of all peaks in Fig. 8(b) was stronger than that in Fig. 8(a), implying that O_2 promoted the adsorption and oxidation of NO. Except for the occurrence of monodenate nitrates (1308 cm^{-1}) and the disappearance of bridged nitrites (1212 cm^{-1}) in Fig. 8(b), there was no significant difference in peak position between Fig. 8(a) and (b).

With the participation of O_3, monodentate nitrates at 1308 cm^{-1} in Fig. 8(b) did not appear in Fig. 8(c), replaced by monodentate nitrates (1253 and 1289 cm^{-1}) and nitro

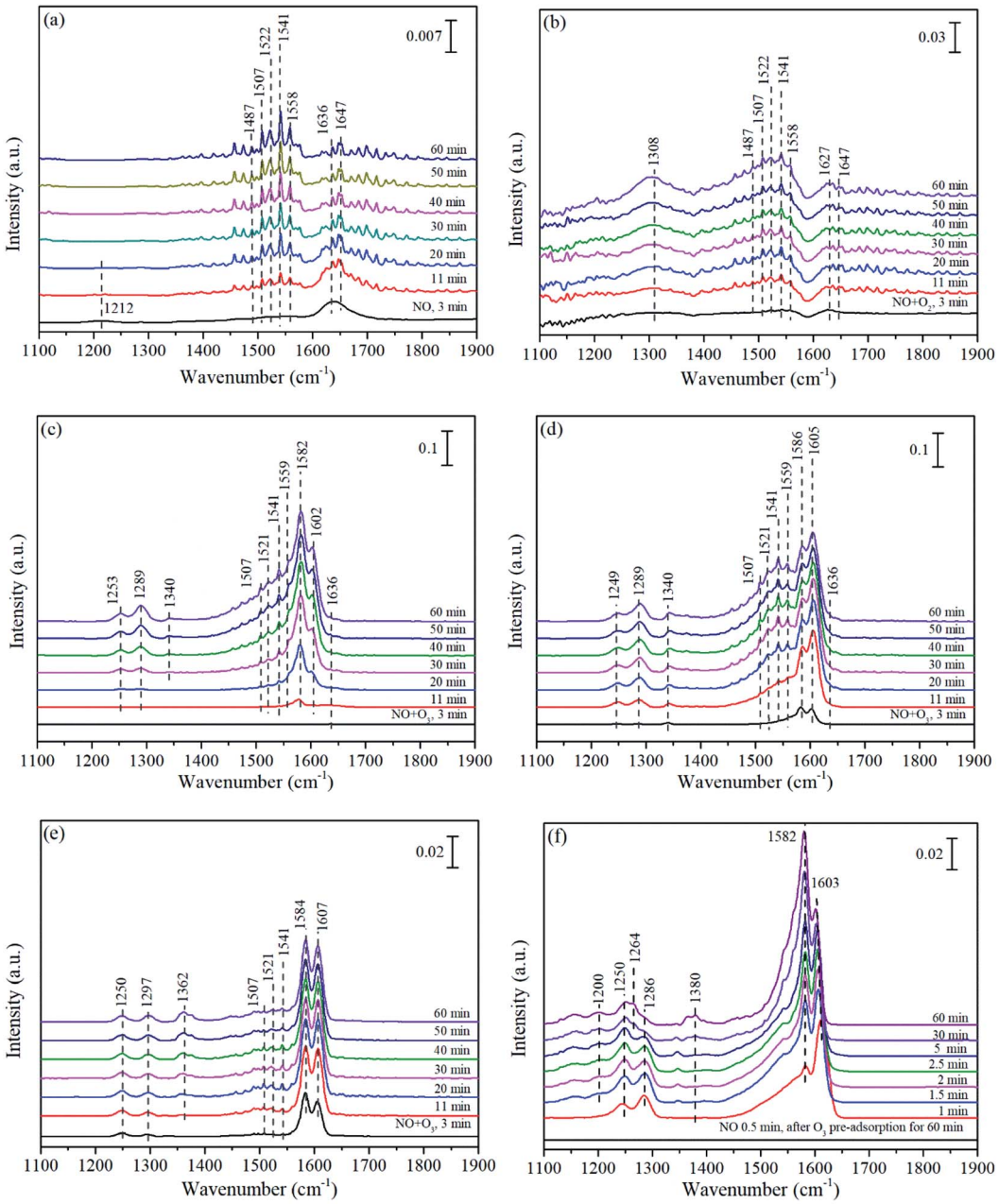

Fig. 8 *In situ* DRIFTS of Mn/TiO_2 (a–d and f) and pure TiO_2 (e) exposed to NO (a), NO + O_2 (b), NO + O_3 at 140 °C (c and e), NO + O_3 at 200 °C (d), and NO after O_3 pre-adsorption at 140 °C (f).

compound (1340 cm^{-1}). Comparing the peak intensity of Fig. 8(b) and (c), similar to the above conclusion could be drawn on Mn/TiO_2 that O_3 further promoted the adsorption and oxidation of NO. Fig. 8(d) showed the co-adsorption behavior of NO + O_3 for Mn/TiO_2 at 200 °C. In comparison with Fig. 8(c), the adsorption bands in Fig. 8(d) reached their highest intensity within 30 min, while it was more than 60 min in Fig. 8(c). It demonstrated that the adsorption–desorption process obtained equilibrium state more quickly on Mn/TiO_2 at 200 °C, which was also the reason why Mn/TiO_2 exhibited higher performance at 200 °C than that at 140 °C. Otherwise, the intensity of bidentate nitrates at 1586 cm^{-1} at 200 °C decreased significantly than that at 140 °C, while monodentate nitrates (1289, 1507 and 1521 cm^{-1}) and bridge nitrates (1605 cm^{-1}) were slightly increased in their intensity. As the main intermediate species, the transformation of bidentate nitrates, monodentate nitrates and bridged nitrates promoted the catalytic oxidation of NO and synergistic effect between Mn/TiO_2 and O_3.

Fig. 8(e) showed the spectra of pure TiO_2 exposed to NO + O_3. In Fig. 8(e), two strong peaks of bidentate nitrates (1584 cm^{-1}) and bridged nitrates (1607 cm^{-1}) appeared quickly and grew as the predominant species. In addition, some inconspicuous monodentate nitrates (1250, 1297, 1507 and 1521 cm^{-1}), bidentate nitrates (1541 cm^{-1})[3,72] and nitro compound

($1362\ cm^{-1}$) were also observed. It was worth noting that the peak intensity of Mn/TiO_2 (Fig. 8(c)) was stronger than that on pure TiO_2, especially for monodentate nitrates (1507 and $1521\ cm^{-1}$). This also suggested that the addition of Mn could facilitate the NO adsorption on Mn/TiO_2, probably due to easily accessible multiple oxidation states of Mn, which was conducive to O_3 decomposition into active oxygen, accompanied by the formation of pivotal intermediate species of monodentate nitrates.

The DRIFT spectra of NO adsorption after O_3 pre-adsorption for 60 min was displayed in Fig. 8(f). It could be seen that the bridge nitrates ($1603\ cm^{-1}$) emerged rapidly in 1 min then grew slow, and even weakened with time, while the bidentate nitrates ($1582\ cm^{-1}$) increased and became shaper than bridge nitrates, probably due to the conversion of the former to the later. The monodentate nitrates at $1286\ cm^{-1}$ first increased then decreased and shifted to 1250 and $1264\ cm^{-1}$, which all assigned to monodentate nitrates. Additionally, weakly adsorbed NO species ($1200\ cm^{-1}$)[76] and monodentate nitrites ($1380\ cm^{-1}$) were also observed. Similarly, the intensity of peaks in Fig. 8(f) was much stronger than that in Fig. 8(a), implying the chemically adsorbed oxygen from O_3 decomposition greatly improved the NO adsorption on the surface of Mn/TiO_2.

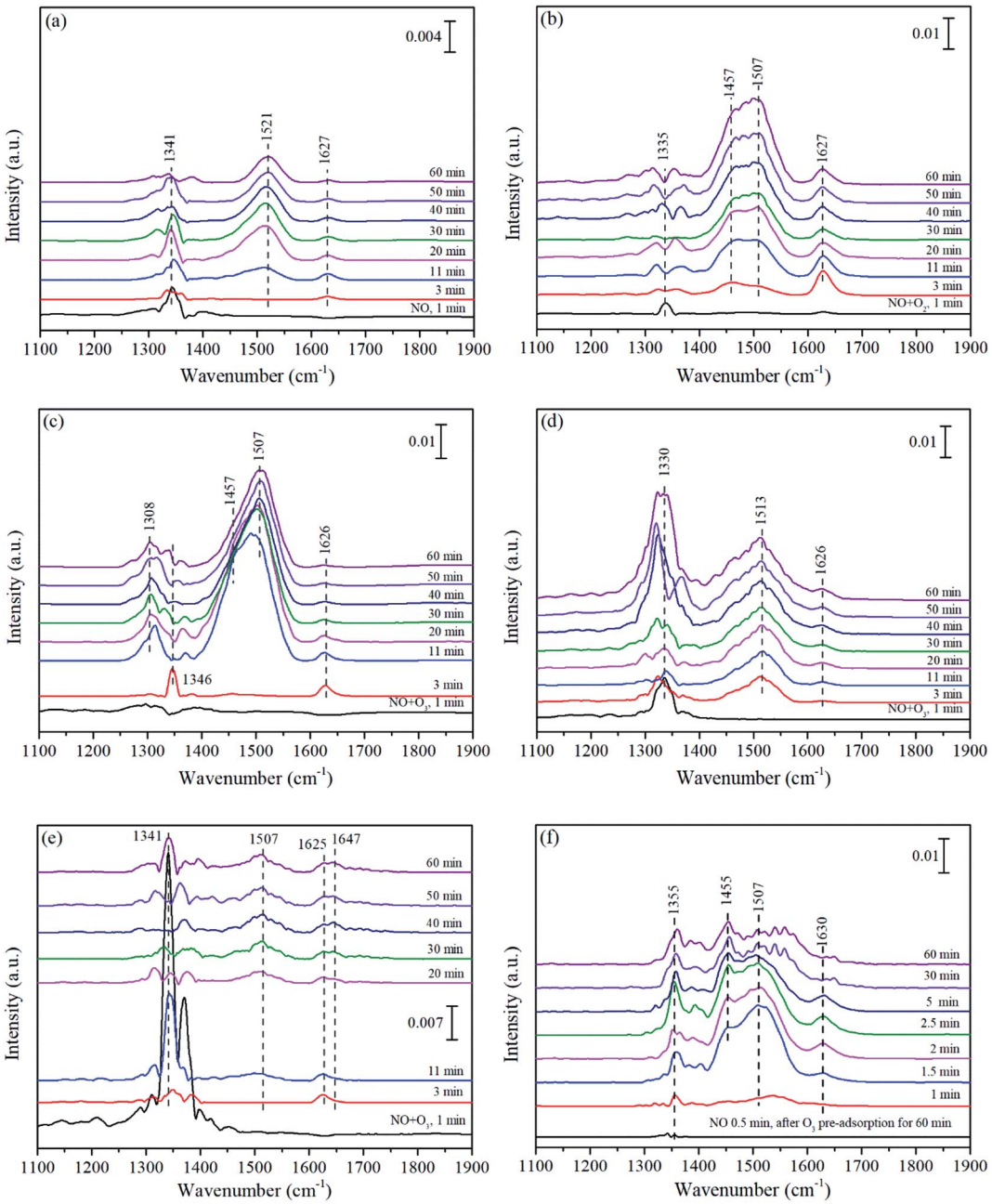

Fig. 9 *In situ* DRIFTS of Mn/MCM-41 (a–d and f) and pure MCM-41 (e) exposed to NO (a), NO + O_2 (b), NO + O_3 at 140 °C (c and e), NO + O_3 at 200 °C (d), and NO after O_3 pre-adsorption at 140 °C (f).

3.3.3 NO adsorption over Mn/MCM-41 catalyst. Similar to the previous experiments, Fig. 9 also showed the adsorption behavior of NO over Mn/MCM-41 and pure MCM-41 under various atmospheres. As shown in Fig. 9(a), nitro compound (1341 cm^{-1}) first appeared within 1 min then fluctuated slightly, and then monodentate nitrates (1521 cm^{-1}) and bridge nitrates (1627 cm^{-1}) gradually appeared. It was worth noting that the monodentate nitrates in Fig. 9(a) grew first then weakened with time, which might be due to the gradual consumption of the active lattice oxygen and not timely replenishment. However, with the participation of O_2 (Fig. 9(b)), monodentate nitrates (1457 cm^{-1})[77] also appeared and the peak intensity of all monodentate nitrates increased gradually with time, which benefited from the active oxygen of O_2. In Fig. 9(c), the nitro compound (1346 cm^{-1}) almost disappeared after 11 min, while monodentate nitrates (1308, 1457 and 1507 cm^{-1}) generated and reached the maximum instantly, which was faster than that in Fig. 9(b), implying that O_3 further accelerated the NO catalytic oxidation on the surface of catalyst. Nevertheless, these nitrates weakened slightly in the following time due to their decomposition.

In Fig. 9(d), monodentate nitrates (1513 cm^{-1}) quickly formed within 3 min, which was faster than that in Fig. 9(c), and then gradually increased. However, the intensity of monodentate nitrates in Fig. 9(d) was lower than that in Fig. 9(c), suggesting that the decomposition of monodentate nitrates was further enhanced at 200 °C and more active sites were released, which in turn promoted the formation of monodentate nitrates, so the monodentate nitrates were continuously generated over time. In combination with the result of Fig. 1(d), it could also be speculated that the highly reactive and easily decomposed monodentate nitrates were an important intermediate species in the catalytic oxidation of NO for Mn/MCM-41.

Fig. 9(e) displayed the adsorption behavior of NO over pure MCM-41 in NO + O_3 at 140 °C. It could be seen from Fig. 9(e) that nitro compound (1341 cm^{-1}) emerged first within 1 min and weakened over time, after that bridged nitrates (1625–1647 cm^{-1}) appeared and reached the maximum intensity in 3 min due to the decomposition of nitro compound. With the consumption of nitro compound and bridged nitrates, monodentate nitrate (1507 cm^{-1}) occurred and grew progressively over time (Fig. 9(e)). However, the intensity of adsorption peaks on pure MCM-41 was very weak, indicating that MCM-41 could only provide very few adsorption sites. Fig. 9(f) showed the *in situ* DRIFT spectra of Mn/MCM-41 exposed to NO after O_3 pre-adsorption for 60 min. All peaks reached the strongest in 2.5 min and then quickly weakened due to the consumption of chemically adsorbed oxygen on the surface of catalyst.

The *in situ* DRIFTS analysis suggested that the adsorption of NO and the formation of nitrates on the surface of catalysts were remarkably promoted by chemically adsorbed oxygen, especially from O_3. Comparing the peak intensities of Mn-based catalysts, the order was as follows: Mn/γ-Al_2O_3 > Mn/TiO_2 > Mn/MCM-41, indicating that the supports had effect on NO adsorption and Mn/γ-Al_2O_3 possessed the best adsorption performance of NO, which was consistent with the activity test in Fig. 1. Nitrates was supposed to the vital intermediate in the formation of NO_2.[78] In comparison with the nitrates intensity of Mn-based catalysts in NO + O_3 at 140 °C (Fig. 7(c), 8(c) and 9(c)), Mn/γ-Al_2O_3 (mainly monodentate and bidentate nitrates) displayed stronger nitrates intensity than that of Mn/TiO_2 and Mn/MCM-41, which might be the reason why the synergistic effect between Mn/γ-Al_2O_3 and O_3 was significantly higher than that between Mn/TiO_2 and O_3, and between Mn/MCM-41 and O_3. Besides, the Mn-based catalysts showed better NO adsorption performance than the corresponding pure supports. Under the interaction between Mn and corresponding supports, the NO adsorption and oxidation was further promoted, probably due to the formation of more active sites with the addition of Mn. According to the characterization analyses, the Mn^{3+} usually generated the oxygen vacancies,[55] which contributed to the excellent activity.[52] O_3 were adsorbed on the oxygen vacancies to form adsorbed oxygen during the electrons transfer between Mn^{3+} and Mn^{4+}, resulting in more active oxygen for the adsorption and activation of NO to form nitrates, and then nitrates decomposed into NO_2.[27,78–80] Therefore, more coexistence of Mn^{3+} and Mn^{4+} as well as more adsorbed oxygen benefited to the NO oxidation. Based on the results of H_2-TPR and XPS, Mn/γ-Al_2O_3 catalyst possessed high content of Mn^{3+} and Mn^{4+} as well as amount adsorbed oxygen, which was conductive to its excellent NO adsorption performance and further improved its catalytic activity.

3.4 NO-TPD analysis

Fig. 10 displayed the NO-TPD profiles of catalysts and the corresponding supports. The desorption peaks below 300 °C was attributed to the monodentate nitrates and bridged nitrates, while the high temperature peaks above 300 °C was assigned to the bidentate nitrates and bridged nitrates.[81] It could be seen that the Mn-based catalysts possessed larger desorption area of NO than the corresponding supports, and desorption peaks were also shifted to the low temperature, indicating that the addition of Mn contributed to the formation and desorption of N-species. In addition, Mn/γ-Al_2O_3 had the largest value and lowest initial desorption temperature among three Mn-based catalysts, suggesting that the surface of

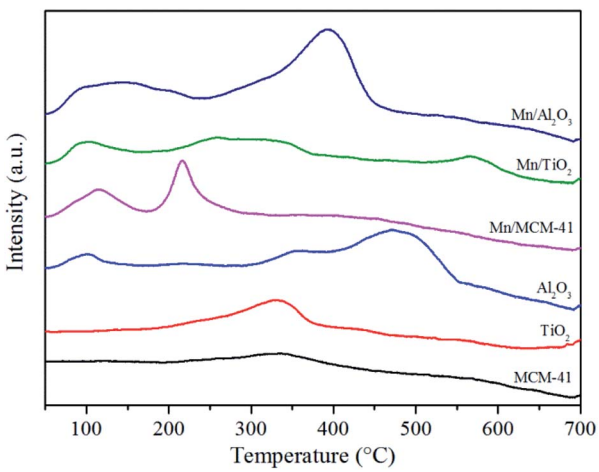

Fig. 10 NO-TPD profiles of the Mn/γ-Al_2O_3, Mn/TiO_2, Mn/MCM-41 and the corresponding supports.

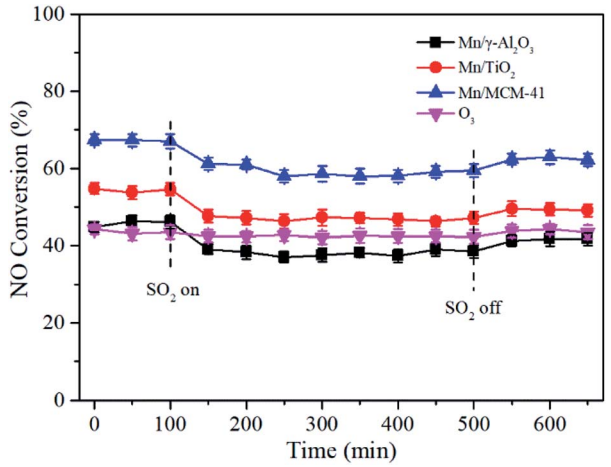

Fig. 11 Effect of SO_2 on NO conversion over Mn/γ-Al_2O_3, Mn/TiO_2, and Mn/MCM-41 catalysts. Reaction conditions: NO = 500 ppm, O_2 = 5 vol%, GHSV = 24 000 h^{-1}, T = 140 °C, O_3/NO = 0.5, SO_2 = 300 ppm.

Mn/γ-Al_2O_3 was most favorable for NO desorption, which was also consistent with that Mn/γ-Al_2O_3 had the strongest NO adsorption capacity (Section 3.3). Interestingly, there were two obvious desorption peaks of monodentate nitrates and bridged nitrates for Mn/MCM-41 at low temperature, consisting with the results of Fig. 9. It demonstrated that NO could be easily desorbed from Mn/MCM-41, but because of the limited adsorption capacity of Mn/MCM-41 for NO, Mn/MCM-41 still did not show high activity.

3.5 Effect of SO_2 on NO conversion

Since SO_2 existed in the exhaust, it was critical to investigate the influence of SO_2 on NO conversion. As shown in Fig. 11, after SO_2 was added into the feed gas, the NO conversion of Mn/γ-Al_2O_3, Mn/TiO_2 and Mn/MCM-41 rapidly decreased by about 8%, and then stabilized at 58%, 46% and 38%, respectively. With the removal of SO_2, NO conversion recovered to a certain extent, but not to the initial state, probably due to the passivation of SO_2 that metal sulfates formed on the surface of catalyst and occupied part of the active sites. However, SO_2 had little effect on NO oxidation by O_3 alone. Except Mn/MCM-41, Mn/γ-Al_2O_3 and Mn/TiO_2 catalysts still showed better performance than O_3 alone, especially Mn/γ-Al_2O_3, suggesting that Mn/γ-Al_2O_3 showed better SO_2 tolerance in the presence of O_3.

4. Conclusions

Mn/γ-Al_2O_3, Mn/TiO_2 and Mn/MCM-41 catalysts were compared for NO catalytic oxidation with low ratio of O_3/NO (O_3/NO < 1) at low temperatures of 80–200 °C. The NO conversion for three catalysts were in the order of Mn/γ-Al_2O_3 > Mn/TiO_2 > Mn/MCM-41. Moreover, there was a clear synergistic effect between Mn/γ-Al_2O_3 and O_3, followed by Mn/TiO_2 and O_3, while for Mn/MCM-41, almost no synergistic effect occurred between Mn/MCM-41 and O_3. The characterization results of XRD, EDS mappings, BET, H_2-TPR, XPS and TG showed that Mn/γ-Al_2O_3 possessed good manganese dispersion, excellent redox performance, abundant chemically adsorbed oxygen and the coexistence of Mn^{3+} and Mn^{4+} in a proper amount, which were the vital factors that contributed to its high activity. The *in situ* DRIFTS results indicated that the chemically adsorbed oxygen species produced by O_3 decomposition greatly promoted the adsorption of NO as well as the formation of nitrates on the catalyst surface. Meanwhile, the Mn-based catalysts showed stronger adsorption bands than the corresponding pure supports. Besides, it also showed that pure γ-Al_2O_3 support provided amount active sites for NO adsorption. Under the interaction between Mn and γ-Al_2O_3, Mn/γ-Al_2O_3 had the strongest NO adsorption performance among three catalysts and greatly accelerated the formation of monodentate nitrates and bidentate nitrates, which were the vital intermediate species for NO_2 formation and further ensured excellent catalytic activity of Mn/γ-Al_2O_3. The NO-TPD outcomes also showed that the Mn-based catalysts showed stronger desorption bands than the corresponding pure supports, and Mn/γ-Al_2O_3 had the best NO desorption performance among three catalysts. The excellent NO adsorption, conversion and desorption performance of Mn/γ-Al_2O_3, all contributed to the high activity of Mn/γ-Al_2O_3. In addition, Mn/γ-Al_2O_3 also exhibited excellent SO_2 tolerance.

Conflicts of interest

There are no conflicts to declare.

Acknowledgements

The project was supported by National Key Research and Development Program of China (2018YFB0605101), Research Fund of International Young Scientists (51550110237), and the Science and Technology Key Project of Tianjin, China (19ZXSZSN00050 and 19ZXSZSN00070), Innovation funding project for Postgraduates in Hebei Province in 2020 (CXZZBS2020035).

References

1 G. Cheng, X. Liu, X. Song, X. Chen, W. Dai, R. Yuan and X. Fu, *Appl. Catal., B*, 2020, **277**, 119196.
2 X. Hou, J. Qian, L. Li, F. Wang, B. Li, F. He, M. Fan, Z. Tong, L. Dong and L. Dong, *Ind. Eng. Chem. Res.*, 2018, **57**, 16675–16683.
3 F. Gao, X. Tang, H. Yi, C. Chu, N. Li, J. Li and S. Zhao, *Chem. Eng. J.*, 2017, **322**, 525–537.
4 H. Chen, Y. Wang and Y.-K. Lyu, *Mol. Catal.*, 2018, **454**, 21–29.
5 Y. Wan, W. Zhao, Y. Tang, L. Li, H. Wang, Y. Cui, J. Gu, Y. Li and J. Shi, *Appl. Catal., B*, 2014, **148–149**, 114–122.
6 A. Wang, Y. Guo, F. Gao and C. H. F. Peden, *Appl. Catal., B*, 2017, **202**, 706–714.
7 B. Wang, H. Su and S. Yao, *Process Saf. Environ. Prot.*, 2020, **133**, 216–223.
8 S. Xie, L. Li, L. Jin, Y. Wu, H. Liu, Q. Qin, X. Wei, J. Liu, L. Dong and B. Li, *Appl. Surf. Sci.*, 2020, **515**, 146014.

9 W. Wang, W. Li, R. Guo, Q. Chen, Q. Wang, W. Pan and G. Hu, *J. Rare Earths*, 2016, **34**, 876–881.
10 Z. Wang, F. Lin, S. Jiang, K. Qiu, M. Kuang, R. Whiddon and K. Cen, *Fuel*, 2016, **166**, 352–360.
11 J. Shao, F. Lin, Y. Huang, Z. Wang, Y. Li, G. Chen and K. Cen, *Appl. Surf. Sci.*, 2020, **503**, 144064.
12 H. Wang, H. Chen, Y. Wang and Y.-K. Lyu, *Chem. Eng. J.*, 2019, **361**, 1161–1172.
13 B. Hao, Y. Sun, Q. Shen, X. Zhang and Z. Zhang, *Chemosphere*, 2020, **243**, 125406.
14 M. L. Saladino, E. Kraleva, S. Todorova, A. Spinella, G. Nasillo and E. Caponetti, *J. Alloys Compd.*, 2011, **509**, 8798–8803.
15 B. Zhao, R. Ran, X. Wu, D. Weng, X. Wu and C. Huang, *Catal. Commun.*, 2014, **56**, 36–40.
16 M. Jin, J. H. Kim, J. M. Kim, J.-K. Jeon, J. Jurng, G.-N. Bae and Y.-K. Park, *Catal. Today*, 2013, **204**, 108–113.
17 X. Tang, F. Gao, Y. Xiang, H. Yi and S. Zhao, *Catal. Commun.*, 2015, **64**, 12–17.
18 S. Thampy, Y. Zheng, S. Dillon, C. Liu, Y. Jangjou, Y.-J. Lee, W. S. Epling, K. Xiong, Y. J. Chabal, K. Cho and J. W. P. Hsu, *Catal. Today*, 2018, **310**, 195–201.
19 Z. Wu, N. Tang, L. Xiao, Y. Liu and H. Wang, *J. Colloid Interface Sci.*, 2010, **352**, 143–148.
20 L. Wang, H. He, C. Zhang, Y. Wang and B. Zhang, *Chem. Eng. J.*, 2016, **288**, 406–413.
21 R. Huang, B. Lan, Z. Chen, H. Yan, Q. Zhang, J. Bing and L. Li, *Chem. Eng. J.*, 2012, **180**, 19–24.
22 H. Einaga and S. Futamura, *Appl. Catal., B*, 2005, **60**, 49–55.
23 J. Shao, Y. Yang, R. Whiddon, Z. Wang, F. Lin, Y. He, S. Kumar and K. Cen, *Energy Fuels*, 2019, **33**, 4454–4461.
24 Z. Han, J. Wang, T. Zou, D. Zhao, C. Gao, J. Dong and X. Pan, *Energy Fuels*, 2020, **34**, 2080–2088.
25 J. Nawrocki and B. Kasprzyk-Hordern, *Appl. Catal., B*, 2010, **99**, 27–42.
26 M. T. N. Dinh, J.-M. Giraudon, A. M. Vandenbroucke, R. Morent, N. de Geyter and J.-F. Lamonier, *Appl. Catal., B*, 2015, **172–173**, 65–72.
27 F. Lin, Z. Wang, Q. Ma, Y. Yang, R. Whiddon, Y. Zhu and K. Cen, *Appl. Catal., B*, 2016, **198**, 100–111.
28 M. Sui, J. Liu and L. Sheng, *Appl. Catal., B*, 2011, **106**, 195–203.
29 Y. Liu, W. Yang, P. Zhang and J. Zhang, *Appl. Surf. Sci.*, 2018, **442**, 640–649.
30 E. Rezaei, J. Soltan and N. Chen, *Appl. Catal., B*, 2013, **136–137**, 239–247.
31 H. Einaga, N. Maeda, S. Yamamoto and Y. Teraoka, *Catal. Today*, 2015, **245**, 22–27.
32 B. Zhu, X.-S. Li, P. Sun, J.-L. Liu, X.-Y. Ma, X. Zhu and A.-M. Zhu, *Chin. J. Catal.*, 2017, **38**, 1759–1769.
33 I. Jõgi, K. Erme, J. Raud and M. Laan, *Fuel*, 2016, **173**, 45–51.
34 F. Lin, Z. Wang, J. Shao, D. Yuan, Y. He, Y. Zhu and K. Cen, *Chin. J. Catal.*, 2017, **38**, 1270–1280.
35 B. M. Reddy and A. Khan, *Catal. Rev.*, 2005, **47**, 257–296.
36 V. K. Patel and S. Sharma, *Catal. Today*, 2020, **71**, 53.
37 L. Qu, C. Li, G. Zeng, M. Zhang, M. Fu, J. Ma, F. Zhan and D. Luo, *Chem. Eng. J.*, 2014, **242**, 76–85.
38 G. A. R. L. McCormick, *Catal. Today*, 2000, **55**, 269–280.
39 R. Cui, S. Ma, J. Wang and S. Sun, *Chemosphere*, 2019, **234**, 302–309.
40 E. Rezaei and J. Soltan, *Chem. Eng. J.*, 2012, **198–199**, 482–490.
41 R. Jin, Y. Liu, Z. Wu, H. Wang and T. Gu, *Chemosphere*, 2010, **78**, 1160–1166.
42 P. G. Smirniotis, P. M. Sreekanth, D. A. Peña and R. G. Jenkins, *Ind. Eng. Chem. Res.*, 2006, **45**, 6436–6443.
43 D. Wang, H. Li, Q. Yao, S. Hui and Y. Niu, *Green Energy Environ.*, 2020, **225**, 134.
44 D. Wang, Q. Yao, S. Liu, S. Hui and Y. Niu, *J. Energy Inst.*, 2019, **92**, 1852–1863.
45 K. H. P. Reddy, B.-S. Kim, S. S. Lam, S.-C. Jung, J. Song and Y.-K. Park, *Environ. Res.*, 2021, **195**, 110876.
46 H. W. Ryu, M. Y. Song, J. S. Park, J. M. Kim, S.-C. Jung, J. Song, B.-J. Kim and Y.-K. Park, *Environ. Res.*, 2019, **172**, 649–657.
47 A. Jankowska, A. Chłopek, A. Kowalczyk, M. Rutkowska, W. Mozgawa, M. Michalik, S. Liu and L. Chmielarz, *Microporous Mesoporous Mater*, 2021, **315**, 110920.
48 J. Li, J. Guo, X. Shi, X. Wen, Y. Chu and S. Yuan, *Appl. Surf. Sci.*, 2020, **534**, 147592.
49 D. Wang, Q. Yao, C. Mou, S. Hui and Y. Niu, *Fuel*, 2019, **254**, 115719.
50 G. S. Pozan, *J. Hazard. Mater.*, 2012, **221–222**, 124–130.
51 J. Li, L. Li, W. Cheng, F. Wu, X. Lu and Z. Li, *Chem. Eng. J.*, 2014, **244**, 59–67.
52 Q. Shen, L. Zhang, N. Sun, H. Wang, L. Zhong, C. He, W. Wei and Y. Sun, *Chem. Eng. J.*, 2017, **322**, 46–55.
53 L. Liu, B. Wang, X. Yao, L. Yang, W. Jiang and X. Jiang, *Fuel*, 2021, **283**, 119336.
54 D. Fang, J. Xie, H. Hu, H. Yang, F. He and Z. Fu, *Chem. Eng. J.*, 2015, **271**, 23–30.
55 X. Zhang, H. Zhao, Z. Song, W. Liu, J. Zhao, Z. a. Ma, M. Zhao and Y. Xing, *Appl. Surf. Sci.*, 2019, **493**, 9–17.
56 J. Liu, R. Guo, M. Li, P. Sun, S. Liu, W. Pan, S. Liu and X. Sun, *Fuel*, 2018, **223**, 385–393.
57 C. Alessandro and I. Valerio, *J. Catal.*, 1974, **33**, 493–496.
58 S. Ma, X. Wang, T. Chen and Z. Yuan, *Chem. Eng. J.*, 2018, **354**, 191–196.
59 X. Chen, Z. Zhao, S. Liu, J. Huang, J. Xie, Y. Zhou, Z. Pan and H. Lu, *J. Rare Earths*, 2020, **38**, 175–181.
60 C. Reed, Y.-K. Lee and S. T. Oyama, *J. Phys. Chem. B*, 2006, **110**, 4207–4216.
61 F. Gao, X. Tang, H. Yi, S. Zhao, W. Zhu and Y. Shi, *J. Environ. Sci.*, 2020, **89**, 145–155.
62 W. Li and F. Fu, *Microporous Mesoporous Mater.*, 2020, **298**, 110060.
63 N. I. Cuello, V. R. Elías, C. E. Rodriguez Torres, M. E. Crivello, M. I. Oliva and G. A. Eimer, *Microporous Mesoporous Mater.*, 2015, **203**, 106–115.
64 Q. Chen, R. Guo, Q. Wang, W. Pan, W. Wang, N. Yang, C. Lu and S. Wang, *Fuel*, 2016, **181**, 852–858.
65 J. Jia, P. Zhang and L. Chen, *Appl. Catal., B*, 2016, **189**, 210–218.

66 V. P. Santos, M. F. R. Pereira, J. J. M. Órfão and J. L. Figueiredo, *Top. Catal.*, 2009, **52**, 470–481.
67 B. Zhao, R. Ran, X. Wu and D. Weng, *Appl. Catal., A*, 2016, **514**, 24–34.
68 K. I. Hadjiivanov, *Catal. Rev.*, 2000, **42**, 71–144.
69 L. Li, Q. shen, J. Cheng and Z. Hao, *Catal. Today*, 2010, **158**, 361–369.
70 X. Yao, L. Chen, J. Cao, Y. Chen, M. Tian, F. Yang, J. Sun, C. Tang and L. Dong, *Chem. Eng. J.*, 2019, **369**, 46–56.
71 G. Qi and W. Li, *Catal. Today*, 2015, **258**, 205–213.
72 Z. Fan, J.-W. Shi, C. Gao, G. Gao, B. Wang, Y. Wang, C. He and C. Niu, *Chem. Eng. J.*, 2018, **348**, 820–830.
73 W. Li, H. Liu, M. Zhang and Y. Chen, *RSC Adv.*, 2019, **9**, 31035–31042.
74 Y. Huang, Y. Yang, H. Hu, M. Xu, H. Liu, X. Li, X. Wang and H. Yao, *Proc. Combust. Inst.*, 2019, **37**, 2951–2957.
75 Y. Xie, Y. Chen, Y. Ma and Z. Jin, *J. Hazard. Mater.*, 2011, **195**, 223–229.
76 E. Gao, H. Pan, W. Zhang, Y. Li, G. Cao, M. T. Bernards, Y. He and Y. Shi, *Chem. Eng. J.*, 2020, **386**, 123956.
77 L. Wei, S. Cui, H. Guo and L. Zhang, *Comput. Mater. Sci.*, 2018, **144**, 216–222.
78 N. Tang, Y. Liu, H. Wang and Z. Wu, *J. Phys. Chem. C*, 2011, **115**, 8214–8220.
79 F. Gao, C. Chu, W. Zhu, X. Tang, H. Yi and R. Zhang, *Appl. Surf. Sci.*, 2019, **479**, 548–556.
80 Y. Liu and P. Zhang, *Appl. Catal., A*, 2017, **530**, 102–110.
81 W. Cai, Y. Zhao, M. Chen, X. Jiang, H. Wang, M. Ou, S. Wan and Q. Zhong, *Chem. Eng. J.*, 2018, **333**, 414–422.